Communication

Polarization-Sensitive Quantum Optical Coherence Tomography: Birefringence Profiles of Biological Samples

Vitaly Sukharenko * and Roger Dorsinville

The City College, City University of New York, 160 Convent Avenue, New York, NY 10031, USA; rdorsinville@ccny.cuny.edu
* Correspondence: vsukharenko@ccny.cuny.edu

Abstract: Polarization-sensitive quantum optical coherence tomography (PS-QOCT) is used to image and characterize birefringence effects in biological samples. Entangled photons are generated via spontaneous parametric down-conversion and split into a reference arm and a sample arm of a Mach Zehnder interferometer. Interferometric patterns between two entangled photons reveal information about tissue birefringence. Biological tissue samples are imaged and characterized, and their quantum interference patterns and birefringence profiles are presented.

Keywords: polarization-sensitive quantum optical coherence tomography; quantum imaging; quantum entanglement; spontaneous parametric down-conversion

1. Introduction

Quantum Optical Coherence Tomography (QOCT) is a technique that incorporates Optical Coherence Tomography (OCT) principles with entangled photons to achieve enhanced imaging capabilities. Classical OCT is a well-established non-invasive imaging modality used in medical and biological applications. The technique utilizes low-coherence interferometry to image samples of interest with micron-scale resolution. A broadband light source is split into two arms: a reference arm and a sample arm. Measuring classical interference between the two beams reveals transverse and cross-sectional images of a sample [1]. In QOCT, entangled photons are generated via spontaneous parametric down-conversion in a non-linear crystal. QOCT employs fourth-order interference, otherwise known as the "photon bunching" effect, to capture and reconstruct the profile of the sample [2–8]. The quantum interference effect is inherently different from classical and offers a reduction of the wave dispersion and is expected to improve image quality and resolution [9–14]. Polarization-Sensitive Quantum Optical Coherence Tomography (PS-QOCT) extends the capabilities of QOCT by providing additional information about polarization and enables measurement and visualization of tissue birefringence [15–18]. In our paper, we present experimental PS-QOCT imaging and characterization of a biological sample.

Classical optical techniques were used in [19–21] to image carcinoma cells of lung tissue via Polarization-Sensitive Optical Coherence Tomography (PS-OCT). The authors reported a birefringence signature. In this work, we use PS-QOCT to image and characterize birefringence in similar histological samples.

Polarization-Sensitive Quantum Optical Coherence Tomography (PS-QOCT) is a fourth-order interferometric technique that uses quantum-entangled photons [15,16]. PS-QOCT eliminates dispersion and enhances the resolution capability that is present in classical OCT [14]. A brief overview of the dispersion cancelation effect in quantum interference is outlined in the next section. The technique provides both axial and transverse optical sectioning capabilities that are also polarization-sensitive. In the experimental setup, entangled photon pairs undergo fourth-order quantum interference in a Mach Zehnder interferometer. In the presence of localized birefringence, interference patterns

change, and these changes are used to image and characterize birefringence within the biological samples.

2. Materials and Methods

2.1. Polarization in Quantum Interference

Figure 1 shows the quantum interference pattern between entangled photons in a Mach Zehnder interferometer obtained by scanning the reference arm relative to the sample arm while measuring the coincidence rate [17]. In a dispersionless sample, the wavenumber of the entangled photons remains unchanged, and the interference profile resembles the standard Hong-Ou-Mandel dip, displayed in Figure 1, scan of a blank microscope slide. For a dispersive medium, we express the wavenumber $k(\omega)$ in the Taylor series about the center wavelength of the entangled photons ω_0 and the down-converted shifted frequency ω:

$$k(\omega) = k_0 + \alpha(\omega - \omega_0) + \beta(\omega - \omega_0)^2 + \dots \tag{1}$$

and approximating the group velocity with the first two terms

$$v_g \simeq 1/\alpha - 2\beta(\omega - \omega_0)/\alpha^2 \tag{2}$$
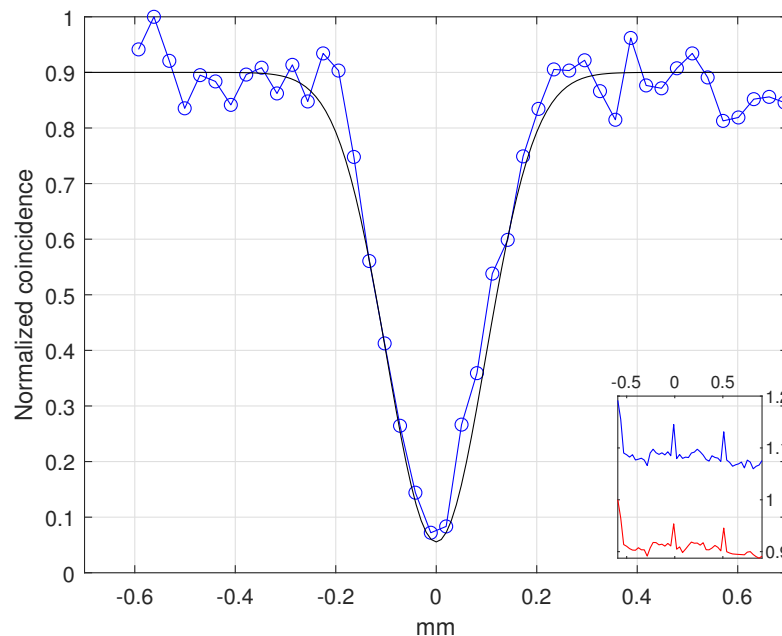
Figure 1. Normalized coincidences, HOM interference pattern. The sub-graph shows single counts.

The annihilation operators corresponding to the two output ports of a 50:50 fiber beam splitter are then described as [14]

$$a_1(\omega_1) = |s\rangle \frac{i}{\sqrt{2}} \sqrt{R} a_s(\omega_1) e^{ik(\omega_1)d} + |r\rangle \frac{1}{\sqrt{2}} \sqrt{T} a_i(\omega_1) e^{i\omega_1 \delta l/c}$$

$$a_2(\omega_2) = |s\rangle \frac{1}{\sqrt{2}} \sqrt{T} a_s(\omega_2) e^{ik(\omega_2)d} + |r\rangle \frac{i}{\sqrt{2}} \sqrt{R} a_i(\omega_2) e^{i\omega_2 \delta l/c} \tag{3}$$

where a_i and a_s are the reference arm and signal arm operators, d is the sample thickness, δl the optical path length translation along the direction of propagation, and $|s\rangle$ is the Jones vector that describes the polarization profile of the sample photons after the birefringent medium and $|r\rangle$ is the Jones vector of the reference beam. In an isotropic medium $|s\rangle \equiv |r\rangle$, all sample photons have the same polarization as the reference photons. T and R are the transmission and reflection coefficients where $T + R = 1$ [2]. The probability of detecting a coincidence between the two detectors is:

$$P_c \propto \int d\omega_1 \int d\omega_2 \langle \Psi | a_1^\dagger(\omega_1) a_2^\dagger(\omega_2) a_1(\omega_1) a_2(\omega_2) | \Psi \rangle \tag{4}$$

Substitution of Equations (1) and (3) into Equation (4) and considering the canonical commutation relation of the operators

$$\langle \Psi | a_1^\dagger(\omega_1) a_2^\dagger(\omega_2) a_1(\omega_1) a_2(\omega_2) | \Psi \rangle =$$

$$\frac{1}{4} R^2 \langle r,s|r,s \rangle a_i^\dagger(\omega_1) a_s^\dagger(\omega_2) a_i(\omega_1) a_s(\omega_2) +$$

$$\frac{1}{4} T^2 \langle s,r|s,r \rangle a_s^\dagger(\omega_1) a_i^\dagger(\omega_2) a_s(\omega_1) a_s(\omega_2)$$

$$+ \frac{1}{4} RT \langle r,s|s,r \rangle a_i^\dagger(\omega_1) a_s^\dagger(\omega_2) a_s(\omega_1) a_s(\omega_2) e^{id(k(\omega_1)-k(\omega_2))+i\delta l/c(\omega_2-\omega_1)}$$

$$+ \frac{1}{4} TR \langle s,r|r,s \rangle a_s^\dagger(\omega_1) a_i^\dagger(\omega_2) a_i(\omega_1) a_s(\omega_2) e^{id(k(\omega_2)-k(\omega_1))+i\delta l/c(\omega_1-\omega_2)} \tag{5}$$

re-writing $\omega' = \omega_1 - \omega_0 = \omega_0 - \omega_2$, also the coincidence window is much larger than the bandwidth of the entangled photons the time integral yields an effective δ function [14]:

$$= \frac{1}{4} |\delta(\omega_p - \omega_1 - \omega_2)|^2 |f(\omega')|^2 [R^2 + T^2$$

$$- 2RT \langle s,r|r,s \rangle cos(2\omega'(\delta l/c - \alpha d))] \tag{6}$$

The function f describes the spectral profile of the down-converted light and is proportional to the coherence of the entangled photons emitted from the crystal. The coincidence rate is:

$$P_c \propto \int d\omega' |f(\omega')|^2 [R^2 + T^2 - 2RT \langle s,r|r,s \rangle cos(2\omega'(\delta l/c - \alpha d))] \tag{7}$$

The second term responsible for the group velocity dispersion, the term containing β, is effectively canceled. The interference dip is centered around $\delta l/c = \alpha d$. The interference profile is defined by the coherence times of the photons emitted from the crystal $|f(\omega')|^2$ and the polarization projection of signal and reference photons. The above expression is identical to Hong-Ou-Mandel dip [2] in a dispersionless medium, where $\langle s,r|r,s \rangle = 1$ all signal photons are of the same polarization as reference photons.

In the case of strong birefringence where signal and reference photons are of orthogonal polarization $\langle s,r|r,s \rangle = 0$ third term in Equation (7) is canceled, and the probability of detecting coincidence is uniform regardless of the scanning position and δl the optical path length difference, Figure 2.

The ratio between two images, first at the interference dip where $\delta l/c = \alpha d$ and second far outside the interference $\delta l/c > \alpha d$, where the third term in Equation (7) is effectively zero, normalizes and highlights the effects of the birefringence profile, while simultaneously minimizes classical noise effects, such as scattering and absorption; for a balanced beam splitter, the ratio is simplified to

$$N_c \propto \int d\omega' \frac{|f(\omega')|^2 [R^2 + T^2 - 2RT \langle s,r|r,s \rangle]}{|f(\omega')|^2 [R^2 + T^2]}$$

$$N_c \propto \int d\omega' \frac{[0.5 - 0.5 \langle s,r|r,s \rangle]}{0.5}$$

$$N_c \propto 1 - \langle s,r|r,s \rangle \tag{8}$$

In a homogeneous and dispersionless medium, the sample and reference photons are of the same polarization, and the normalized coefficient is zero, while in the highly birefringent sample, the polarization of the entangled photons is orthogonal, and the normalized coefficient is one. This is the central result of our paper. In the next sections, we scanned biological tissue samples and imaged the birefringence and normalized coefficient.
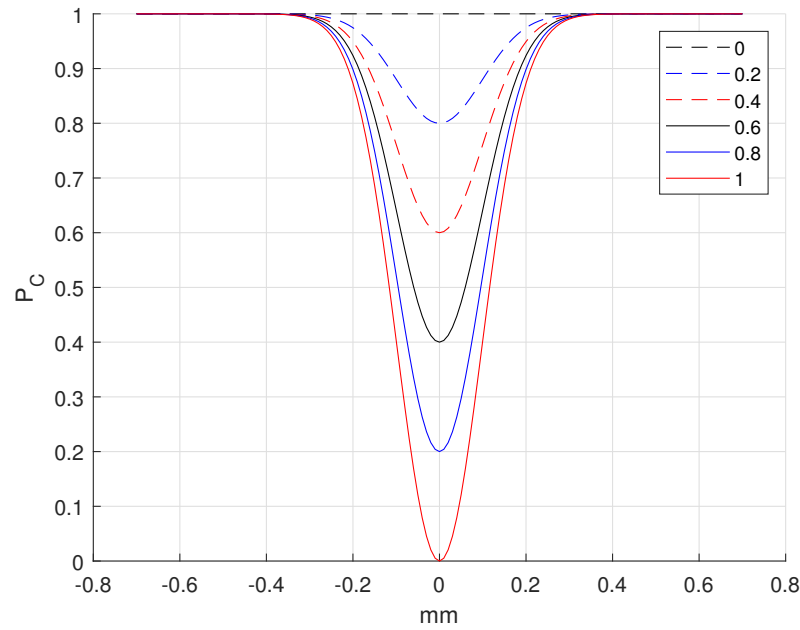
Figure 2. Quantum Interference with polarization projection of signal and reference photons between 0 and 1.

2.2. Experimental Setup

The experimental setup is shown in Figure 3. A continuous wavelength, single longitudinal mode laser diode with a center wavelength at 405 nm is focused onto a PP-KTP (KTiOPO$_4$), type II crystal. Entangled photons centered at 810 nm are generated via Spontaneous Parametric Down-Conversion SPDC. Entangled photon pairs have orthogonal polarization and are emitted in a semi-colinear configuration with the pump. A dichroic mirror (DM) transmits SPDC photons and reflects the pump photons. At the polarizing beam splitter (PBS), the down-converted photon pairs are separated by polarization into the two arms of a Mach Zehnder interferometer.
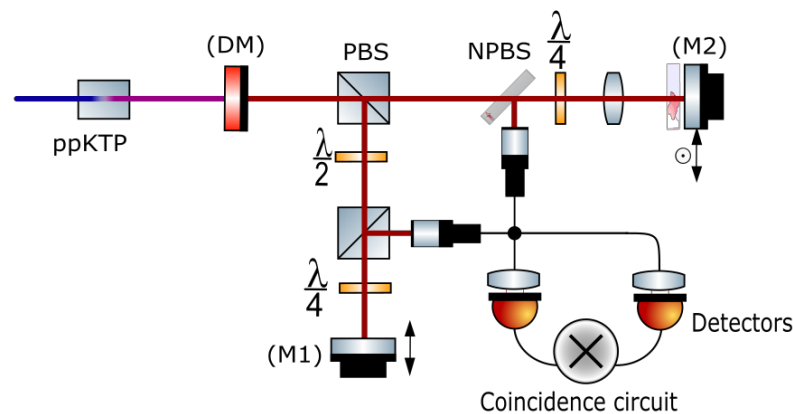
**Figure 3.** Experimental setup for Polarization-Sensitive Quantum Optical Coherence Tomography.

The s-polarized photons are directed towards a moveable delay mirror (M1). The (M1) mirror is scanned along the direction of propagation during the experiment to match the path length of the other sample arm, preserving indistinguishability and ensuring interference of entangled photons. S-polarized photons are reflected from the PBS and directed into a single mode, non-polarizing 50:50 fiber optic coupler.

The horizontally polarized sample arm photons are transmitted through the first PBS and directed towards a non-polarizing beam splitter (NPBS). The NPBS has a 50:50 reflection/transmission ratio and transmits half of the entangled photons toward a mirror

(M2). A microscope slide with the biological tissue is placed against the (M2) mirror for transverse plane scanning. The QWP converts the polarization of the photons into circularly polarized photons, followed by a 20mm focusing lens. The sample and mirror combination reflects photons towards the NPBS, where they are directed into a single mode, non-polarizing 50:50 fiber optic coupler. The photons from the delayed and sample arms are recombined in the fiber optic coupler. The delay arm mirror is scanned along the direction of propagation to match the path length of the sample arm. When entangled photons between two arms are indistinguishable in propagation path and polarization, quantum interference is observed using a coincidence circuit. Two single photon counting modules, along with the coincidence circuit (denoted $\otimes$), measure the coincidence rate of the entangled photons.

3. Results

The histopathological melanoma lung tissue samples, 7 μm thick, were obtained from Carolina Biological Supply Company, PO Box 6010, Burlington NC 27216, USA item 317768. The samples were sandwiched between a glass slide and a cover slip. The cover slip was secured to the slide with an adhesive. The samples were stained with hematoxylin and eosin. Figures 4a,b,f, and 5a are photos of the tissue samples. A number of biological tissue samples were purchased at different times and scanned in the same manner, to confirm the repeatability of the birefringent profiles imaged using the PS-QOCT technique.
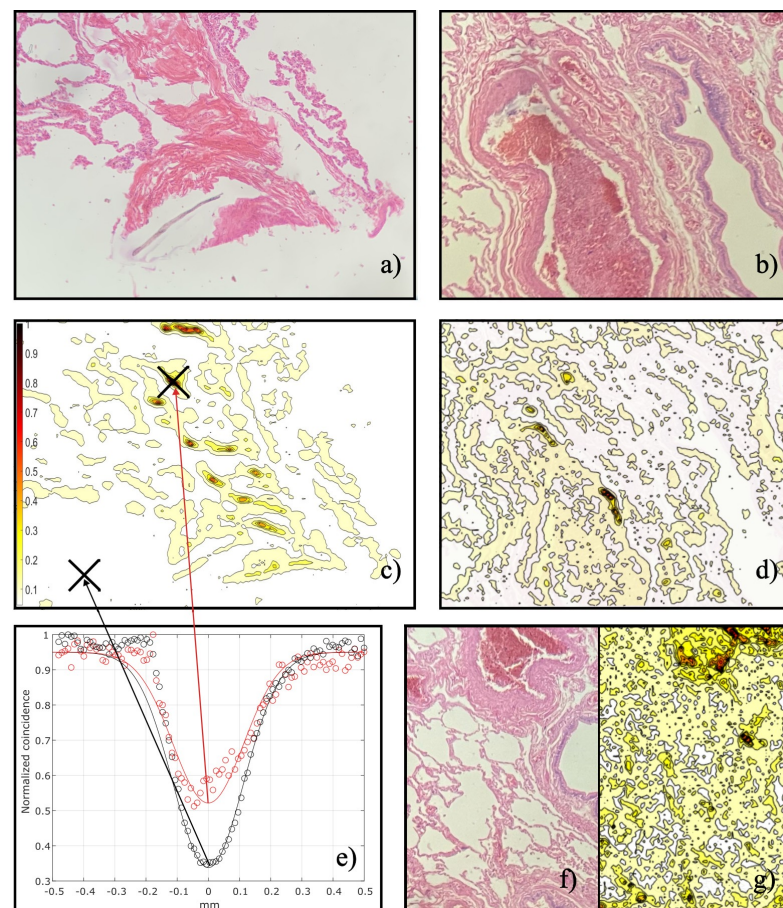
Figure 4. (**a**) histopathological melanoma lung tissue sample No. 1, (**b**) melanoma lung tissue sample No. 2, (**c**) birefringence profile of the sample No. 1, (**d**) birefringence profile of the sample No. 2, (**e**) quantum interference profiles between glass and tissue in sample No. 1, (**f**) melanoma lung tissue sample No. 3, (**g**) birefringence profile of the sample No. 3.

The biological sample slide is fixed to the (M2) mirror and scanned in a transverse plane with 10 μm resolution while recording coincidence counts of the entangled photons. The 10 μm resolution is estimated from the diameter of the entangled beam and the 20 mm focusing lens. The area of interest (1 mm × 1.2 mm) was scanned twice: first at the interference dip where $\delta l / c = \alpha d$ and second far outside the interference $\delta l / c > \alpha d$. The ratio between two images normalizes and highlights the effects of the birefringence profile while simultaneously minimizing classical noise effects, such as scattering and absorption. Scanning results are shown in Figures 4c,d,g and 5b. Figure 5c includes a gradient scale applicable to all normalized birefringent profiles and represents a degree to which the sample arm photons differ in polarization from their counterparts, the reference arm photons. Profiles in Figure 5c are exceptions and correspond to a separate arbitrary unit scale. Localized birefringence in the sample alters entangled photons polarization, reducing their indistinguishability. Reduced indistinguishability, in turn, changes the coincidence rate and minimizes the projection coefficient along with the visibility of the Hong-Ou-Mandel dip, as shown in Figure 4e and as captured in the normalized birefringence profiles.

Next, we explore the transverse imaging of the biological samples and associated birefringence profiles along the direction of photon propagation. The CW arrangement described above with the 10 mm ppKTP crystal and a highly coherent pump generates entangled photons with FWHM interference pattern, Figure 1, of ∼350 μm much wider compared to the sample thickness of 7 μm. Images were obtained for five different points around $\delta l / c = \alpha d$ within the interference dip. The investigated area is shown in Figure 5a,b, and the associated profiles are shown in Figure 5c. High contrast signifies higher birefringence effects in the tissue. Most optimal profiles, with greater visibility, were obtained closest to the center of the interference dip, where $\delta l / c = \alpha d$. As the (M1) mirror moves further from the $\delta l / c = \alpha d$, the reconstructed birefringence pattern degrades and ultimately completely disappears outside of the Hong-Ou-Mandel dip, Equation (8).
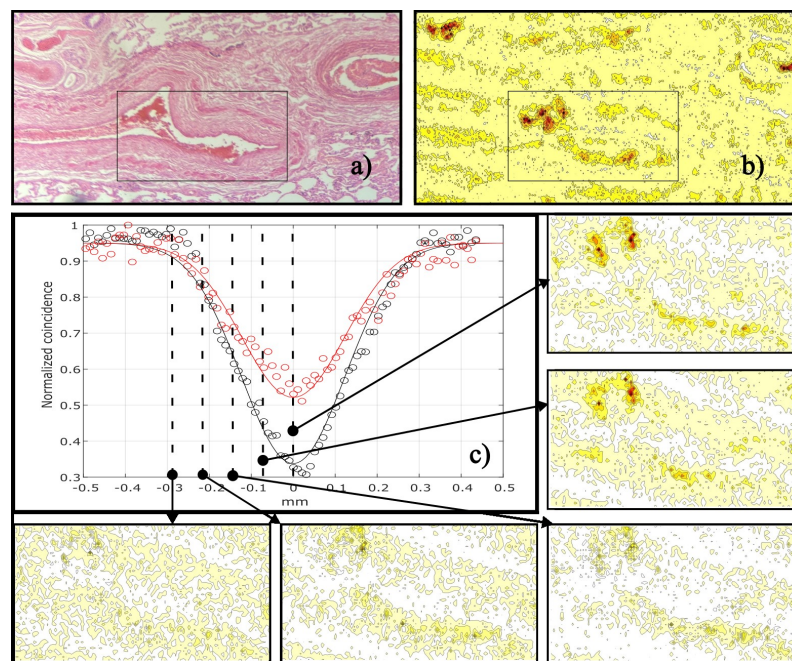
Figure 5. (**a**) Melanoma lung tissue sample No. 4, (**b**) birefringence profile of sample No. 4, (**c**) sectional birefringence profiles at various points of the quantum interference profile.

4. Discussion

In this study, we introduce an experimental technique for Polarization-Sensitive Quantum Optical Coherence Tomography (PS-QOCT) imaging and characterization of biological birefringent samples. Our investigation delves into the exploration of birefringence profiles. Notably, Figure 4 illustrates normalized profiles derived from three distinct melanoma

lung tissue samples, each subjected to scans conducted weeks apart. The results exhibit a remarkable level of repeatability and consistency.

Figure 4c specifically displays the birefringence profile for tissue Figure 4a, featuring a gradient scale aligned with the normalized projection coefficient outlined in Equations (7) and (8). In regions beyond the tissue, such as the microscope glass slide, where the medium is both homogeneous and dispersionless, the polarization difference between the sample and reference photons converges effectively to zero.

Additionally, Figure 4d illustrates the birefringence profile for the tissue in Figure 4b, and the corresponding profile Figure 4g pertains to the sample in Figure 4f. Further insights are offered by profiles along the direction of photon propagation within the sample, as depicted in Figure 5. Notably, we emphasize the indispensability of the quantum interference effect for imaging birefringence. Optimal images, characterized by the highest contrast manifest at the central point of quantum interference, where $\delta l / c = \alpha d$.

The presented technique holds considerable promise for various applications in the characterization of biological samples, as well as micro and nanostructures. This innovative approach contributes to advancing our understanding and opening up new possibilities for imaging and analysis.

References

1. Tripathi, R. Polarization-sensitive optical coherence tomography: A review of classical and quantum perspectives. *Quantum Inf. Process.* **2012**, *11*, 1533–1549. [CrossRef]
2. Hong, C.K.; Ou, Z.Y.; Mandel, L. Measurement of subpicosecond time intervals between two photons by interference. *Phys. Rev. Lett.* **1987**, *59*, 2044. [CrossRef] [PubMed]
3. Zhao, Z. Polarization-Sensitive Quantum-Optical Coherence Tomography with Entangled Photons. In Proceedings of the International Conference on Quantum Information 2007, Rochester, NY, USA, 13–15 June 2007.
4. Hayama, K.; Cao, B.; Okamoto, R.; Suezawa, S.; Okano, M.; Takeuchi, S. High-depth-resolution imaging of dispersive samples using quantum optical coherence tomography. *Opt. Lett.* **2022**, *47*, 4949–4952. [CrossRef] [PubMed]
5. Nasr, M.B.; Goode, D.P.; Nguyen, N.; Rong, G.; Yang, L.; Reinhard, B.M.; Saleh, B.E.A.; Teich, M.C. Quantum-optical coherence tomography of a biological sample. *Opt. Commun.* **2009**, *282*, 1154–1159. [CrossRef]
6. Lopez-Mago, D.; Novotny, L. Quantum-Optical Coherence Tomography with Collinear Entangled Photons. *Opt. Lett.* **2012**, *37*, 4077–4079. [CrossRef] [PubMed]
7. Okano, M.; Okamoto, R.; Tanaka, A.; Ishida, S.; Nishizawa, N.; Takeuchi, S. High-resolution Quantum Optical Coherence Tomography by Broadband Parametric Fluorescence. In Proceedings of the Conference on Lasers and Electro-Optics Pacific Rim, OSA, Kyoto, Japan, 30 June–4 July 2013.
8. Okano, M.; Lim, H.; Okamoto, R. 0.54 μm resolution two-photon interference with dispersion cancellation for quantum optical coherence tomography. *Sci. Rep.* **2016**, *5*, 18042. [CrossRef] [PubMed]
9. Nasr, M.B.; Saleh, B.E.A.; Sergienko, A.V.; Teich, M.C. Dispersion-cancelled and dispersion-sensitive quantum optical coherence tomography. *Opt. Express* **2004**, *12*, 1353–1362. [CrossRef] [PubMed]
10. Nasr, M.B.; Saleh, B.E.A.; Sergienko, A.V.; Teich, M.C. Demonstration of Dispersion-Canceled Quantum-Optical Coherence tomography. *Phys. Rev. Lett.* **2003**, *91*, 083601. [CrossRef] [PubMed]
11. Saleh, B.E.A.; Nasr, M.B.; Sergienko, A.V.; Teich, M.C. Dispersion effects in quantum optical coherence tomography. In Proceedings of the Frontiers in Optics 2004, Rochester, NY, USA, 12–15 October 2004.
12. Abouraddy, A.F.; Nasr, M.B.; Saleh, B.E.A.; Sergienko, A.V.; Teich, M.C. Quantum-optical coherence tomography with dispersion cancellation. *Phys. Rev. A* **2002**, *65*, 053817. [CrossRef]
13. Larchuk, T.S.; Teich, M.C.; Saleh, B.E.A. Nonlocal cancellation of dispersive broadening in Mach-Zehnder interferometers. *Phys. Rev. A* **1995**, *52*, 4145–4154. [CrossRef] [PubMed]
14. Steinberg, A.M.; Kwiat, P.G.; Chiao, R.Y. Dispersion cancellation and high-resolution time measurements in a fourth-order optical interferometer. *Phys. Rev. A* **1992**, *45*, 6659. [CrossRef] [PubMed]

15. Booth, M.C.; Giuseppe, G.D.; Saleh, B.E.A.; Sergienko, A.V.; Teich, M.C. Polarization-sensitive quantum-optical coherence tomography. *Phys. Rev. A* **2004**, *69*, 043815. [CrossRef]

16. Booth, M.C.; Saleh, B.E.A.; Teich, M.C. Polarization-sensitive quantum-optical coherence tomography: Experiment. *Opt. Commun.* **2011**, *284*, 2542–2549. [CrossRef]

17. Sukharenko, V.; Bikorimana, S.; Dorsinville, R. Birefringence and scattering characterization using polarization sensitive quantum optical coherence tomography. *Opt. Lett.* **2021**, *46*, 2799–2802. [CrossRef] [PubMed]

18. Sukharenko, V.; Dorsinville, R. Polarization Sensitive Imaging with Qubits. *Appl. Sci.* **2022**, *12*, 2027. [CrossRef]

19. Hariri, L.P.; Villiger, M.; Applegate, M.B.; Mino-Kenudson, M.; Mark, E.J.; Bouma, B.E.; Suter, M.J. Seeing beyond the bronchoscope to increase the diagnostic yield of bronchoscopic biopsy. *Am. J. Respir. Crit. Care Med.* **2013**, *187*, 125–129. [CrossRef] [PubMed]

20. Carriel, V.S.; Aneiros-Fernandez, J.; Arias-Santiago, S.; Garzón, I.J.; Alaminos, M.; Campos, A. A novel histochemical method for a simultaneous staining of melanin and collagen fibers. *J. Histochem. Cytochem.* **2011**, *59*, 270–277. [CrossRef] [PubMed]

21. Patel, R.; Khan, A.; Quinlan, R.; Yaroslavsky, A.N. Polarization-Sensitive Multimodal Imaging for Detecting Breast Cancer. *Cancer Res.* **2014**, *74*, 4685–4693. [CrossRef] [PubMed]